# The Surface Expression of Semidiurnal Internal Tides near a Strong Source at Hawaii. Part II: Interactions with Mesoscale Currents*

C. CHAVANNE, P. FLAMENT, AND D. LUTHER

*School of Ocean and Earth Science and Technology, University of Hawaii at Manoa, Honolulu, Hawaii*

K.-W. GURGEL

*Institute of Oceanography, University of Hamburg, Hamburg, Germany*

ABSTRACT

Observations of semidiurnal surface currents in the Kauai Channel, Hawaii, are interpreted in the light of the interaction of internal tides with energetic surface-intensified mesoscale currents. The impacts on internal tide propagation of a cyclone of 55-km diameter and ~100-m vertical decay scale, as well as of vorticity waves of ~100-km wavelength and 100–200-m vertical decay scales, are investigated using 3D ray tracing. The Doppler-shifted intrinsic frequency is assumed to satisfy the classic hydrostatic internal wave dispersion relation, using the local buoyancy frequency associated with the background currents through thermal-wind or gradient-wind balance. The $M_2$ internal tide rays with initial horizontal wavelength of 50 km and vertical wavelength of $O(1000 \text{ m})$ are propagated from possible generation locations at critical topographic slopes through idealized mesoscale currents approximating the observed currents. Despite the lack of scale separation between the internal waves and background state, which is required by the ray-tracing approximation, the results are qualitatively consistent with observations: the cyclone causes the energy of internal tide rays propagating through its core to increase near the surface (up to a factor of 15), with surfacing time delayed by up to 5 h (~150° phase lag), and the vorticity waves enhance or reduce the energy near the surface, depending on their phase. These examples illustrate the fact that, even close to their generation location, semidiurnal internal tides can become incoherent with astronomical forcing because of the presence of mesoscale variability. Internal tide energy is mainly affected by refraction through the inhomogeneous buoyancy frequency field, with Doppler shifting playing a secondary but not negligible role, inducing energy transfers between the internal tides and background currents. Furthermore, the vertical wavelength can be reduced by a factor of 6 near the surface in the presence of the cyclone, which, combined with the energy amplification, leads to increased vertical shear within the internal tide rays, with implications for internal wave-induced mixing in the ocean.

## 1. Introduction

The purpose of this paper is to investigate the effects of mesoscale currents on internal tide propagation. This is motivated by observations of semidiurnal currents in the Kauai Channel (Chavanne et al. 2010, hereafter Part I) during the Hawaii Ocean Mixing Experiment (HOME; Rudnick et al. 2003; Pinkel and Rudnick 2006). Part I compares the observed coherent (i.e., phase locked with astronomical forcing) semidiurnal currents with numerical predictions of the tides in an ocean at rest. Although the agreement is good for the phase, indicating propagation of internal tides away from the submarine ridge where they are generated in the Kauai Channel, the kinetic energy pattern and magnitude are less well predicted. Furthermore, a complex demodulation of the currents at semidiurnal frequencies reveals significant temporal variability in their amplitude and phase, not only because of the interference between semidiurnal constituents (e.g., spring–neap cycle) but also on shorter and irregular time scales. Part I suggests that some of the observed variability could be attributed to the effects of barotropic background currents on internal tide propagation. However, the HOME observations reveal that
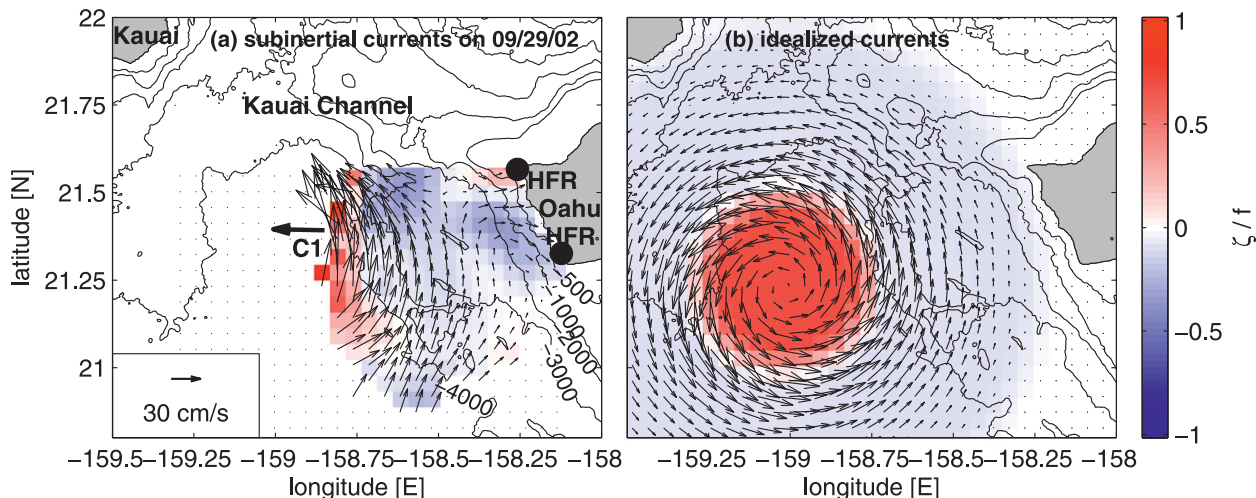
FIG. 1. Surface currents and vorticity (normalized by $f$) for (a) subinertial currents on 29 Sep 2002, observed by HFRs (thin vectors) and an ADCP moored at C1 (12-m depth bin; thick vector) and (b) the idealized Rankine vortex used for ray tracing. Isobaths (thin lines, from 150-m-resolution data; Eakins et al. 2003) are shown at 500, 1000, 2000, 3000, and 4000 m.

highly horizontally and vertically sheared mesoscale currents dominate the subinertial variability in the Kauai Channel and could possibly affect internal tide propagation as well.

Interactions of internal waves with background flows have traditionally been addressed using ray-tracing—or Wentzel–Kramers–Brillouin (WKB)—techniques (e.g., Bretherton 1966; Jones 1969; Müller 1976; Olbers 1981b). This approximation is formally valid as long as the wavelengths are much smaller than the scales of background flow variations, which is usually satisfied for high-frequency internal waves in the atmosphere and ocean. However, internal tides and near-inertial oscillations typically have wavelengths on the order of or even larger than the scales of background flow variations, as is the case for the semidiurnal internal tides in the Kauai Channel (Part I). Although this violates the WKB assumptions, Kunze (1985) showed that ray-tracing results agreed qualitatively with exact numerical solutions for near-inertial waves propagating through horizontally and vertically sheared rectilinear jets, provided the flow scales were not much smaller than the wave scales. This approach neglects scattering effects (Olbers 1981a). Young and Ben Jelloul (1997) developed an approximation for near-inertial frequencies to avoid the scale separation requirement of WKB. However, semidiurnal frequencies are too far from the inertial frequency at the latitude of the Kauai Channel (inertial period ~33 h) to be able to apply the method of Young and Ben Jelloul (1997).

Park and Watts (2006) and Rainville and Pinkel (2006) used ray tracing to study the propagation of internal tides through mesoscale currents in the southwestern Japan/

East Sea and the Hawaiian archipelago, respectively. Their results agreed qualitatively with their observations, despite the marginal scale separation between internal tides and mesoscale currents. They both used a 2D ray-tracing approach to study the effects of mesoscale currents on the horizontal propagation of vertical modes, assuming that the modes propagated independently from each other. Our observations are close to the Hawaiian Ridge, where the strongly varying bottom topography (Fig. 1) couples the vertical modes together (Griffiths and Grimshaw 2007). Even away from the ridge, the modes are coupled by vertically sheared background currents (Mooers 1975a). For this reason, Rainville and Pinkel (2006) only considered barotropic currents and Park and Watts (2006) considered the advective effect of mesoscale currents, averaged above the thermocline, on the mode-1 tide propagation. In the Kauai Channel, the beamlike structure of the internal tides close to the ridge (Martin et al. 2006) warrants the use of a 3D ray-tracing approach.

A traditional approximation consists of neglecting the stratification variability associated with the background currents, retaining only the Doppler-shift effect (e.g., Jones 1969; Müller 1976; Bühler and McIntyre 2005; Polzin 2008). This allows for a simple characterization of the evolution of the wavenumber on the background flow topology. However, results using this approximation (not shown) failed to show a significant impact of mesoscale currents on internal tide propagation in the Kauai Channel. Following Olbers (1981b), Edwards and Staquet (2005), and Moulin and Flór (2006), we retain here the stratification variability associated with the background

currents (assumed to be in thermal- or gradient-wind balance), and we show that it has a significant effect on internal tide propagation in the Kauai Channel. Although we retain the vertical gradient of buoyancy in the dispersion relation (through the buoyancy frequency), we neglect the horizontal gradients of buoyancy and the 3D gradients of background currents when deriving the dispersion relation. The latter gradients appear only in the equations for the evolution of the wave packet position and wavenumber. We furthermore use the hydrostatic approximation. This "standard" WKB technique gives results that are qualitatively consistent with our observations. The inclusion of the current shears and horizontal gradients of buoyancy in the dispersion relation (e.g., Mooers 1975b; Kunze 1985; Jones 2005) is likely to further affect internal tide propagation, through modifications of the Coriolis and buoyancy frequencies "felt" by the waves (effective Coriolis and buoyancy frequencies; Kunze 1985) and through the addition of imaginary terms in the dispersion relation, which correspond to energy exchanges between the waves and the mean flow (Jones 2001). These effects are beyond the scope of the present paper.

The paper is organized as follows: the background currents in which internal tides propagate are described in section 2, and idealized profiles are chosen to obtain the associated stratification through thermal-wind or gradient-wind balance. The results of ray tracing of semidiurnal internal tides through the idealized background currents are analyzed and compared with observations in section 3. The results are summarized and their implications for tidal dissipation and ocean mixing are discussed in section 4. The ray-tracing equations and numerical integration scheme are detailed in the appendix.

## 2. Mesoscale currents

3D ray tracing requires knowledge of the 3D structures of background currents. The horizontal structures were observed by high-frequency radio (HFR) Doppler surface current meters deployed along the west shore of Oahu (Fig. 1a) and are described in section 2a. The vertical structures were observed by moored acoustic Doppler current profilers (ADCPs), deployed in the Kauai Channel (labeled C1 in Fig. 1a and C2 and A2 in Fig. 3a) and are

described in section 2b. The currents were low-pass filtered with a 2-day cutoff period to obtain the subinertial currents. The reader is referred to Part I for details of experimental setting and data processing. Ray tracing also requires knowledge of the 3D structures of stratification, which are inferred in section 2c from thermal-wind or gradient-wind balance, using idealized horizontal and vertical structures for the background currents. We investigate the effects on internal tide propagation of two distinctive mesoscale features that were observed in the Kauai Channel: a cyclone in fall 2002 and vorticity waves in spring 2003.

### a. Horizontal structure

During fall 2002, the low-frequency variability was dominated by mesoscale and submesoscale vortices, such as the cyclone shown in Fig. 1a on 29 September 2002. It was only partially sampled as it drifted into the observational domain from the south before exiting to the west. Velocity reached 70 cm s$^{-1}$ and vorticity $\zeta = \partial v/\partial x - \partial u/\partial y$ reached $0.7f$, but the strongest vorticity inside the core was not sampled. Because the HFR observational domain is quite limited compared with the horizontal extent of the generation locations of internal tides in the Kauai Channel (Carter et al. 2008), we need to extrapolate the measurements over a larger domain. We therefore approximate the observed subinertial circulation on 29 September 2002 by that associated with an isolated axisymmetric cyclone, with characteristics derived from the observed currents. Its center location was estimated from the observed current curvature field, and currents were interpolated onto a polar grid with the origin at the estimated center. Azimuthally averaged currents and vorticity are shown in Fig. 2. The observations (barely) resolve the location of the maximum azimuthal velocity, yielding a radius $R = 27$ km. The vorticity is positive up to 35 km from the center and becomes negative beyond, remaining almost constant around $-0.1f$ beyond 40 km. We idealize the cyclone as an isolated Rankine vortex with a core of constant cyclonic vorticity of radius $R$, surrounded by a ring of constant anticyclonic vorticity of outer radius $L = 3R = 81$ km (Fig. 2), and assume the horizontal and vertical structures are separable:

$$V(r, z) = V_0 F(z) \begin{cases} \dfrac{r}{R} & \text{if} \quad 0 \leq r \leq R, \\[2mm] \dfrac{1}{1 - (R/L)^2}\left[\dfrac{R}{r} - \left(\dfrac{R}{L}\right)^2 \dfrac{r}{R}\right] & \text{if} \quad R \leq r \leq L, \\[2mm] 0 & \text{if} \quad r \geq L, \end{cases} \tag{1}$$
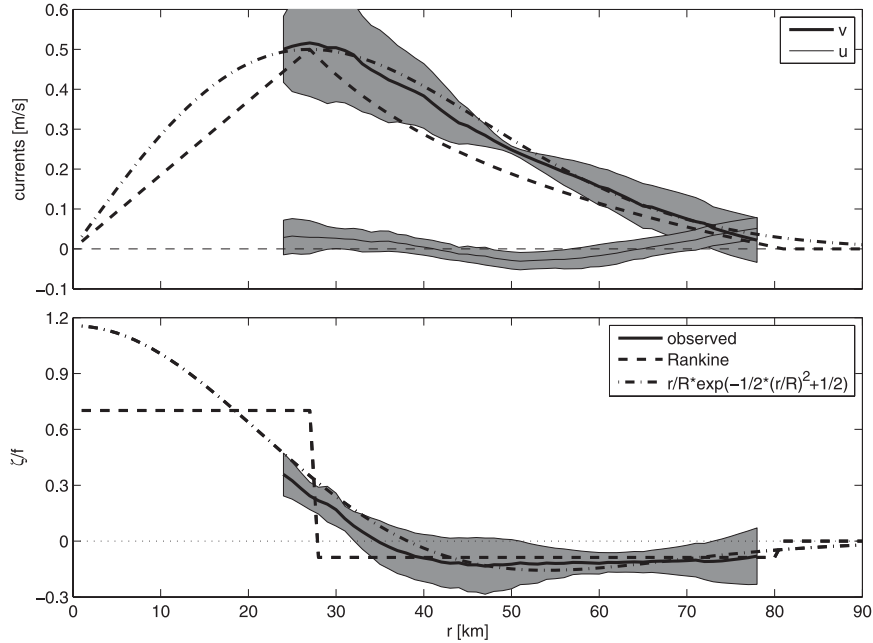
FIG. 2. Azimuthally averaged (solid lines) radial profiles of (top) azimuthal (thick lines) and radial (thin lines) currents and (bottom) vorticity (normalized by $f$) for the cyclone on 29 Sep 2002. Gray shadings indicate ±one standard deviation. Idealized profiles used for ray tracing are superimposed: an isolated Rankine vortex (dashed lines) and a more realistic vortex [Eq. (2); dashed–dotted lines].

where $V_0 = 50$ cm s$^{-1}$ is the vortex maximum current and $F(z)$ is the vertical structure (prescribed in section 2b). The resulting surface patterns are shown in Fig. 1b. Chavanne (2007) also investigated a profile of the form

$$V(r, z) = V_0 F(z) \frac{r}{R} e^{-(1/2)(r/R)^2 + (1/2)}, \qquad (2)$$

which reproduces the observed profile better than the Rankine vortex does (Fig. 2) but is statically unstable near its center.

During spring 2003, the low-frequency variability was dominated by vorticity waves, with northwestward and southeastward alternating currents. These waves had a northeastward phase propagation, and their frequency and wavenumber satisfied the dispersion relation of vortex Rossby waves propagating on the radial gradient of potential vorticity associated with a large cyclone south of Kauai (Chavanne et al. 2010, manuscript submitted to *J. Phys. Oceanogr.*, hereafter CFLG). The waves are shown at two different phases in Fig. 3, on 19 March and 20 April (average currents from 3 March to 1 May were removed). On 19 March, velocity reached 40 cm s$^{-1}$ and vorticity was negative in the entire observational domain (except near the coast), reaching $-0.4\,f$. The wave pattern was almost rectilinear in the southeastern part of the observational domain, but not in the northwestern part, where currents flowed northeastward across the

Kauai Channel. On April 20, velocity reached 30 cm s$^{-1}$ and vorticity ranged from $-0.5f$ near the coast to $0.4f$ offshore. The wave pattern was approximately rectilinear.

We idealize the currents as sinusoidal rectilinear jets for the purpose of ray tracing and neglect the influence of the coast,

$$V(x, z) = V_0 F(z) \cos(kx + \phi), \qquad (3)$$

where $V$ is the velocity component in the direction $y$, perpendicular to the wave propagation direction $x$ (shown by thick dashed lines in Fig. 3); $V_0$ is the maximum velocity; $F(z)$ is the vertical structure (prescribed in section 2b); $k = 2\pi/L$ is the wavenumber; $L$ is the wavelength; and $\phi$ is the phase. The observed current component $V$ in the rotated reference frame, averaged over the area to the southeast of the dashed lines shown in Fig. 3, is well represented by the sinusoidal profiles (Fig. 4), but the observed component $U$ differs significantly from zero. On 19 March, $V_0 = 25$ cm s$^{-1}$ and $L = 100$ km, yielding a vorticity amplitude of $0.3f$ (Figs. 4a,c); on 20 April, $V_0 = 16$ cm s$^{-1}$ and $L = 90$ km, yielding a vorticity amplitude of $0.2f$ (Figs. 4b,d). The velocity amplitude on 20 April was chosen as the maximum velocity yielding stable jets, given the prescribed vertical structure (see sections 2b and 2c), and it is slightly weaker than—but within one standard deviation of—the averaged observed amplitude. The waves are almost 180° out
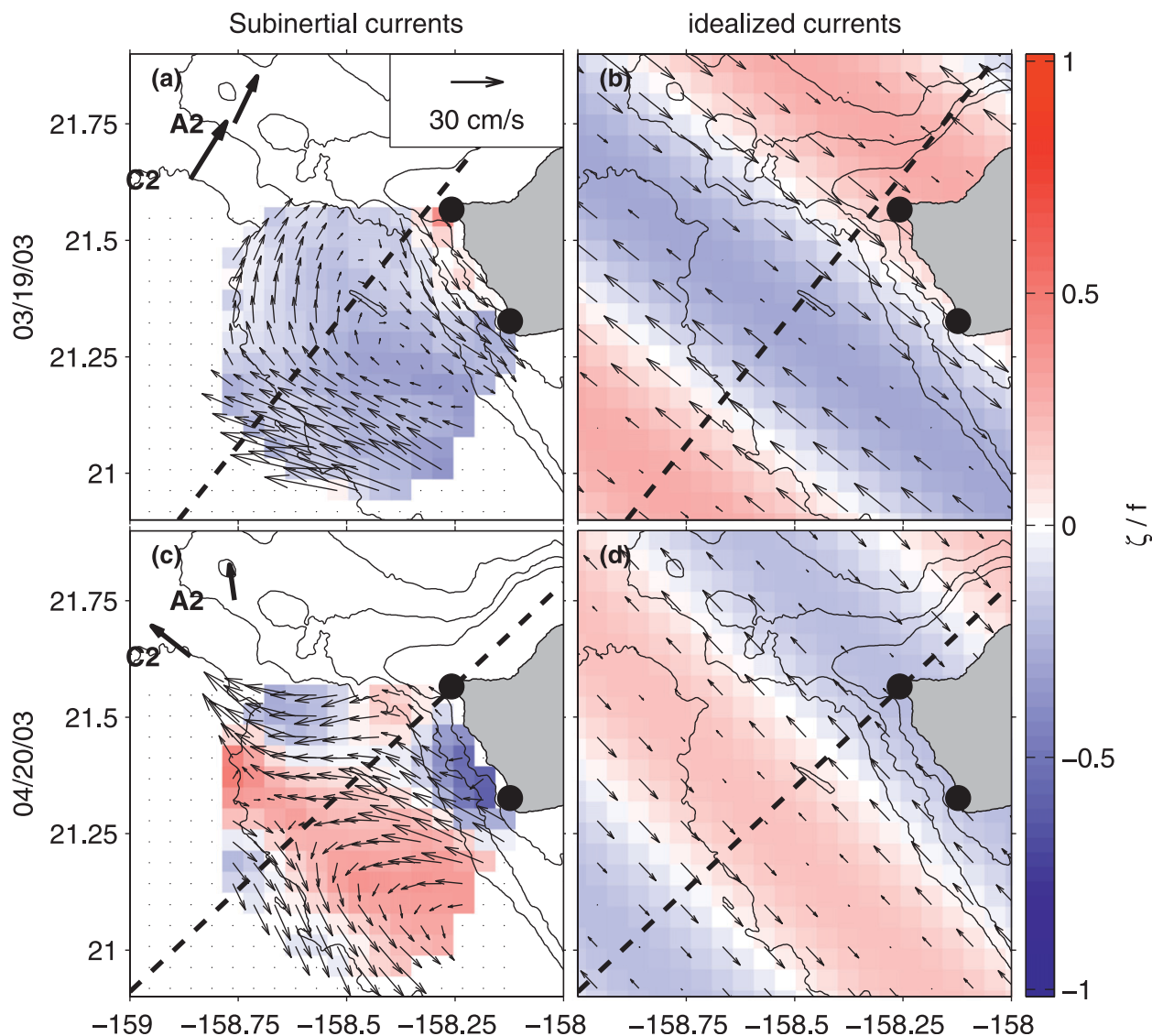
FIG. 3. (left) Observed and (right) idealized subinertial surface current anomalies (average currents from 3 Mar to 1 May were removed) and vorticity (normalized by $f$) on (top) 19 Mar and (bottom) 20 Apr 2003. Observations are from HFRs (thin vectors) and ADCPs moored at C2 and A2 (12-m depth bin; thick vectors). The thick dashed lines indicate the direction of phase propagation of the vorticity waves.

of phase between 19 March and 20 April. The resulting surface patterns are shown in Figs. 3b,d. They are crude approximations to the observed currents but will nevertheless yield qualitative agreement between ray-tracing results and surface semidiurnal current observations, as shown in section 3b.

### b. Vertical structure

The vertical profile of currents at C1 on 29 September 2002 is shown in Fig. 5. Currents are strongly sheared and do not rotate much with depth in the top 100 m. The buoyancy frequency depends on the second vertical derivative of horizontal currents [Eqs. (7) and (10)], and the

vertical refraction of internal waves depends on the vertical gradient of buoyancy frequency [Eq. (A12)], so ray-tracing results are sensitive to the third vertical derivative of currents. Therefore, we cannot directly use the observed vertical structure, which is too noisy. Instead, we choose to fit a smooth analytical profile to the observations, as for the horizontal structures, which also allows us to extrapolate the observed currents over the entire water column. We investigate the sensitivity of the ray-tracing results to the vertical structure of the currents by choosing two different analytical profiles.

An exponential profile is a "natural" choice in the surface quasigeostrophic framework for a single horizontal
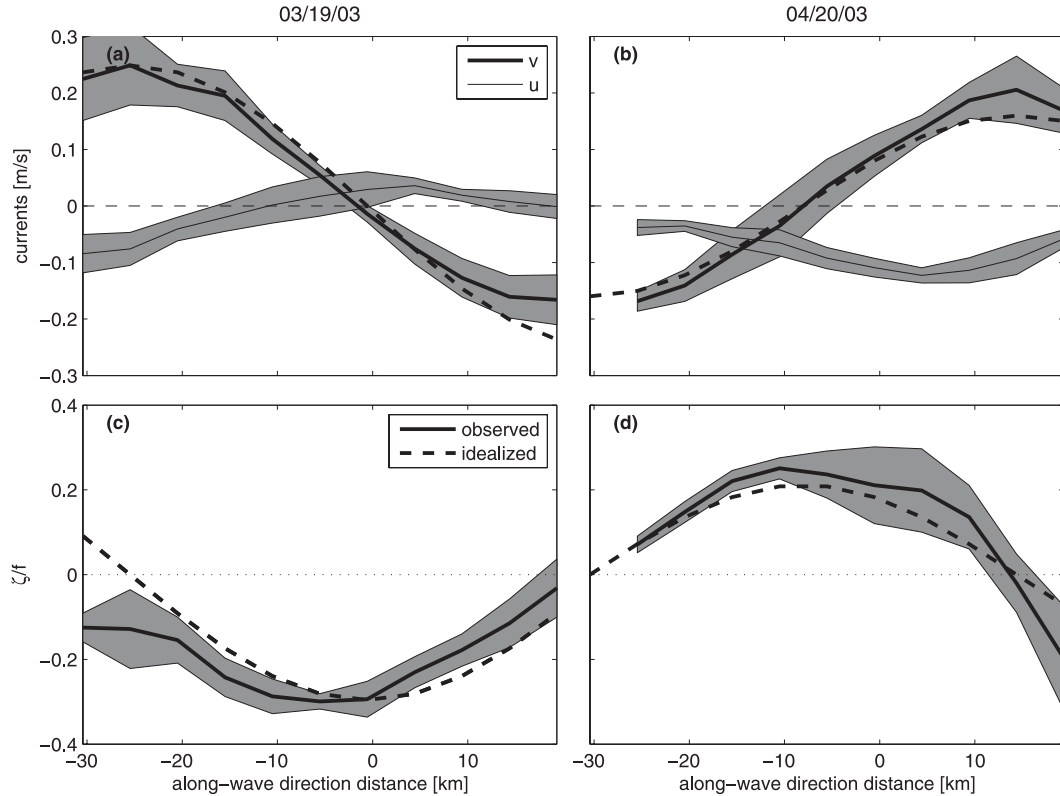
FIG. 4. Profiles (as a function of distance along the direction of phase propagation of the vorticity waves) of (top) currents in the across-propagation direction (thick lines) and along-propagation direction (thin lines) and (bottom) vorticity (normalized by $f$) on (left) 19 Mar and (right) 20 Apr 2003. Observations (solid lines) were averaged over the area to the southeast of the thick dashed lines shown in Fig. 3, and gray shadings indicate ±one standard deviation. Idealized (sinusoidal) profiles used for ray tracing are shown as dashed lines.

spectral Fourier component (Blumen 1978; Held et al. 1995; Lapeyre and Klein 2006),

$$F(z) = e^{z/H}. \tag{4}$$

Here, $H = 95$ m gives the best fit with the observed profile but yields an unstable cyclone with the horizontal structure prescribed in section 2a. As a compromise, we take $H = 150$ m, which yields a stable vortex for maximum horizontal velocity of 24 cm s$^{-1}$, half of that observed (Fig. 2).

To obtain a stable vortex with realistic horizontal velocity, we also use a Gaussian profile,

$$F(z) = e^{-(z/H)^2}, \tag{5}$$

with $H = 95$ m, yielding a stable vortex with the horizontal structure prescribed in section 2a. Furthermore, it reproduces the observed shear better than the exponential profile does in the first 100 m (Fig. 5).

Snapshots of currents at C2 and A2 on 19 March and 20 April (not shown) are not representative of the vorticity

wave vertical structures because they are not aligned perpendicular to the propagation direction (especially on 19 March, when they are aligned parallel to the propagation direction; Fig. 3a). Instead, we use vertical profiles obtained from complex empirical orthogonal function analysis of the currents observed by the HFRs and ADCPs (CFLG), shown in Fig. 6. The similarity of the observed current profiles at C2 and A2 supports the choice of separable horizontal and vertical structures.

The current profile of the vorticity wave on 19 March 2003 can be well approximated by a Gaussian profile [Eq. (5)] with a decay scale $H = 200$ m, yielding a stable wave with the horizontal structure prescribed in section 2a. The vertical profile of the vorticity wave on 20 April 2003 is more complicated. It first slightly increases with depth from the surface down to ~40 m, then it decays sharply down to 100 m, before increasing again to a local maximum around 200 m. We will not try to reproduce the 40- or 200-m maxima, with the near-surface variations being over scales much smaller than the typical internal tide vertical wavelength (see section 3) and the deeper variations not directly affecting the properties of the
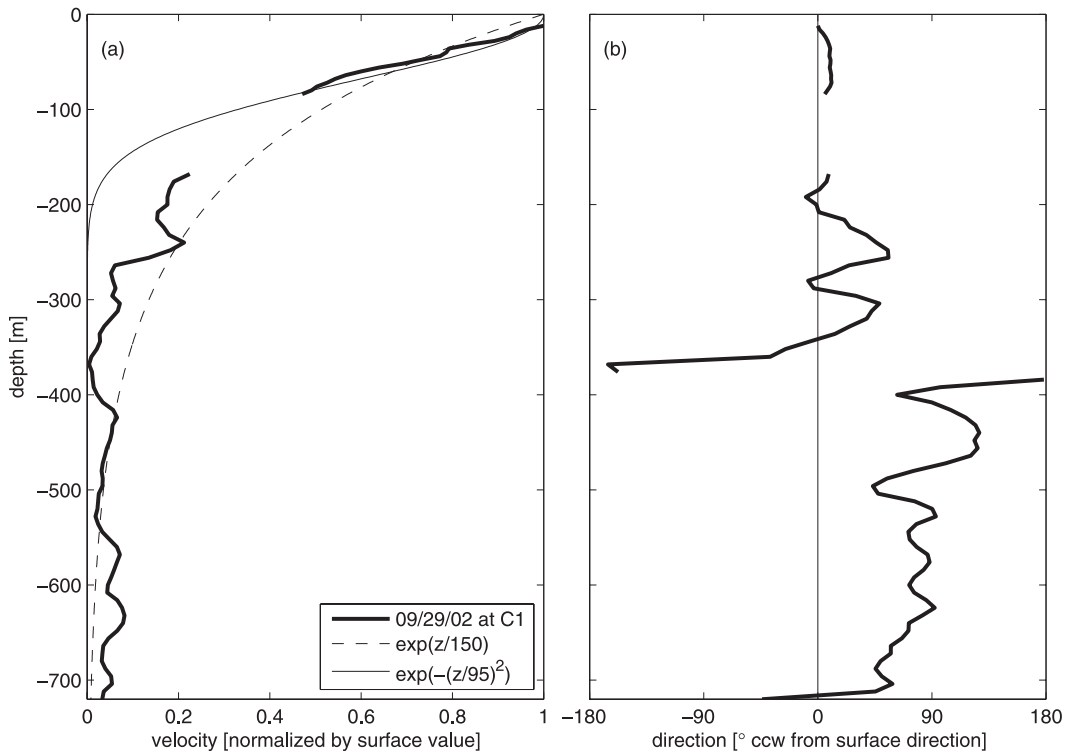
FIG. 5. Vertical profile of horizontal current (a) velocity (normalized by its surface value) and (b) direction (counterclockwise from its surface value), measured by the ADCPs at mooring C1 on 29 Sep 2002 (thick lines) and idealized for ray tracing, using an exponential (thin dashed line) and a Gaussian (thin solid line) decay with depth.

internal tides near the surface. We therefore also use a Gaussian profile with $H = 95$ m, yielding a stable wave for maximum horizontal velocity of 16 cm s$^{-1}$, only slightly weaker than the averaged observed amplitude (Fig. 4b).

### c. Stratification

Because the cyclone has vorticity $\zeta = O(f)$ (Fig. 1), we assume it is in gradient-wind balance, where Coriolis and centrifugal forces balance the pressure gradient force,

$$\frac{g}{\rho_0}\frac{\partial \rho}{\partial r} = -\left(f + \frac{2V}{r}\right)\frac{\partial V}{\partial z}. \qquad (6)$$

Using Eq. (1), Eq. (6) can be solved for $\rho$, from which we can obtain the buoyancy frequency squared $N^2 = -g/\rho_0\ \partial\rho/\partial z$:

$$N^2(r, z) = \begin{cases} N^2(R, z) + \left[\dfrac{fV_0}{R}\dfrac{\partial^2 F}{\partial z^2} + \left(\dfrac{V_0}{R}\right)^2\dfrac{\partial^2 F^2}{\partial z^2}\right]\dfrac{r^2 - R^2}{2} & \text{if}\quad 0 \leq r \leq R, \\[2mm] N_0^2(z) + \dfrac{fR}{2}\dfrac{\partial^2 \tilde{F}}{\partial z^2} - \dfrac{1}{2}\dfrac{\partial^2 \tilde{F}^2}{\partial z^2}\left(\dfrac{R}{r}\right)^2 + \dfrac{1}{2}\left[\dfrac{\partial^2 \tilde{F}^2}{\partial z^2}\left(\dfrac{R}{L}\right)^2 - fR\dfrac{\partial^2 \tilde{F}}{\partial z^2}\right]\left(\dfrac{r}{L}\right)^2 \\[2mm] \quad + \left[2\dfrac{\partial^2 \tilde{F}^2}{\partial z^2}\left(\dfrac{R}{L}\right)^2 - fR\dfrac{\partial^2 \tilde{F}}{\partial z^2}\right]\ln\dfrac{L}{r} & \text{if}\quad R \leq r \leq L, \\[2mm] N_0^2(z) & \text{if}\quad r \geq L, \end{cases} \qquad (7)$$

where $N^2(R, z)$ in the first line can be evaluated from the second line expression; $N_0^2(z)$ is the stratification of the ocean at rest, computed from 10-yr-averaged temperature and salinity observations at Station ALOHA (22.75°N, 158°W; Karl and Lukas 1996), located ~100 km north of Oahu; and $\tilde{F}(z) = V_0/[1 - (R/L)^2]F(z)$.
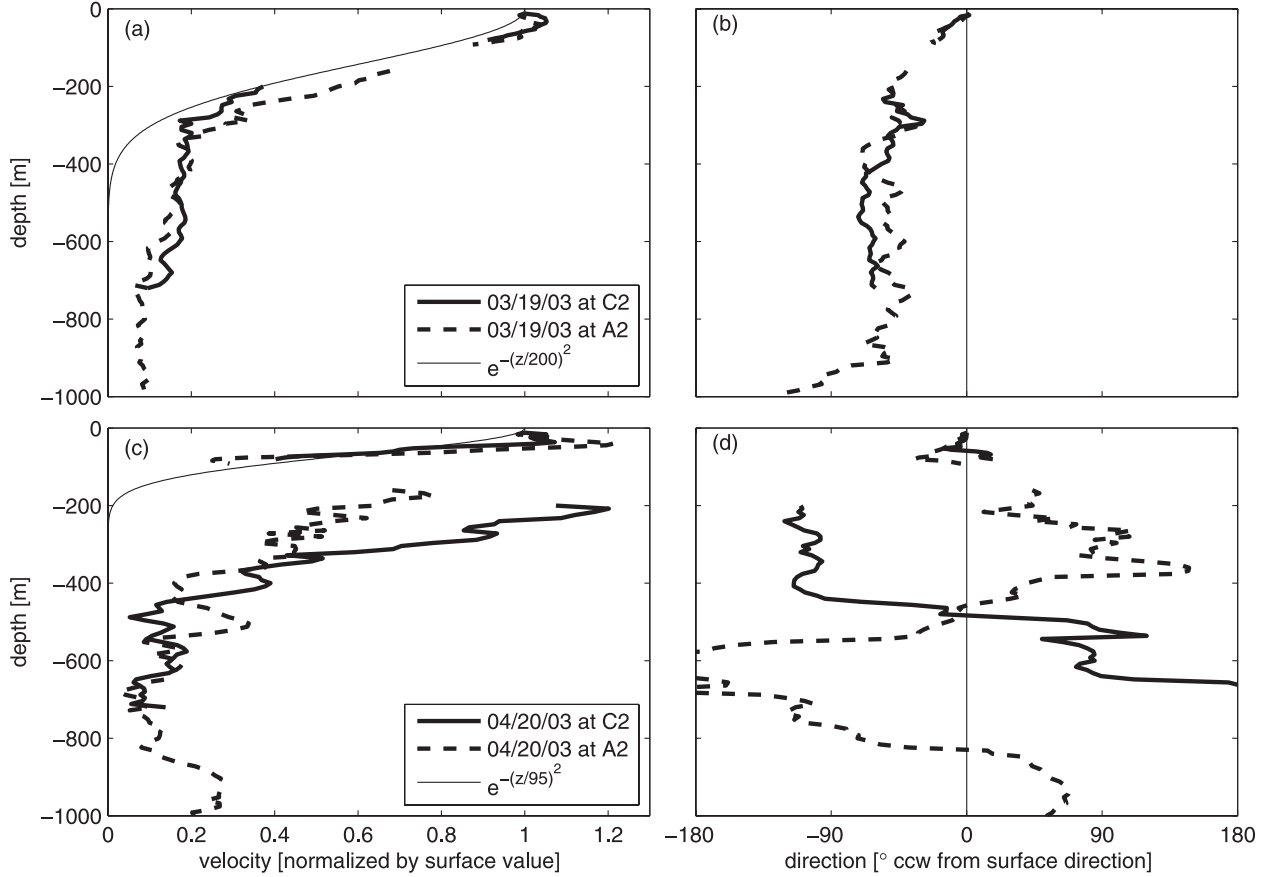
FIG. 6. Vertical profiles of horizontal current (left) velocity (normalized by its surface value) and (right) direction (counterclockwise from its surface value) measured by the ADCPs at mooring C2 (thick solid lines) and A2 (thick dashed lines) for the vorticity wave on (top) 19 Mar and (bottom) 20 Apr 2003. The vertical profiles were obtained from complex empirical orthogonal function analysis of the currents observed by the HFRs and ADCPs. Idealized (Gaussian) profiles used for ray tracing are shown as thin solid lines.

The parameters for the horizontal and vertical structures of the cyclone were chosen to yield an inertially stable vortex (R. Kloosterziel 2008, personal communication),

$$R_i = \frac{N^2}{\left(\frac{\partial V}{\partial z}\right)^2} > \frac{f + 2V/r}{f + \zeta}. \tag{8}$$

The rhs of (8) equals 1 in the core of a solid-body rotating vortex.

The resulting density structure and some buoyancy frequency vertical profiles at different radii are shown for the cyclone with exponential (Figs. 7a,b) and Gaussian (Figs. 7c,d) vertical structures. As expected, stratification is extremely sensitive to the vertical structure of the currents. For the exponential structure, isopycnals outcrop at the surface in the vortex core and the buoyancy frequency is reduced everywhere. For the Gaussian structure, isopycnals do not outcrop at the surface but are stretched below the thermocline and squeezed above it in the vortex

core, resulting in a reduction of buoyancy frequency below the thermocline and an enhancement above it.

We assume that the vorticity waves are in thermal-wind balance, where the Coriolis force balances the pressure gradient force (the nonlinear acceleration terms are zero for rectilinear parallel currents),

$$\frac{g}{\rho_0} \frac{\partial \rho}{\partial x} = -f \frac{\partial V}{\partial z}. \tag{9}$$

Using Eq. (3), Eq. (9) can be solved for $\rho$, yielding the buoyancy frequency squared,

$$N^2(x, z) = N_0^2(z) + \frac{fV_0}{k} \sin(kx + \phi)\frac{\partial^2 F}{\partial z^2}. \tag{10}$$

The reference stratification $N_0(z)$ is chosen to be where the currents are at extrema, so that the buoyancy frequency profiles oscillate around it along the waves (Figs. 7f,h). Stratification is more affected by the vorticity wave on 20 April than on 19 March, because of the stronger vertical shear near the surface on 20 April (Fig. 6).
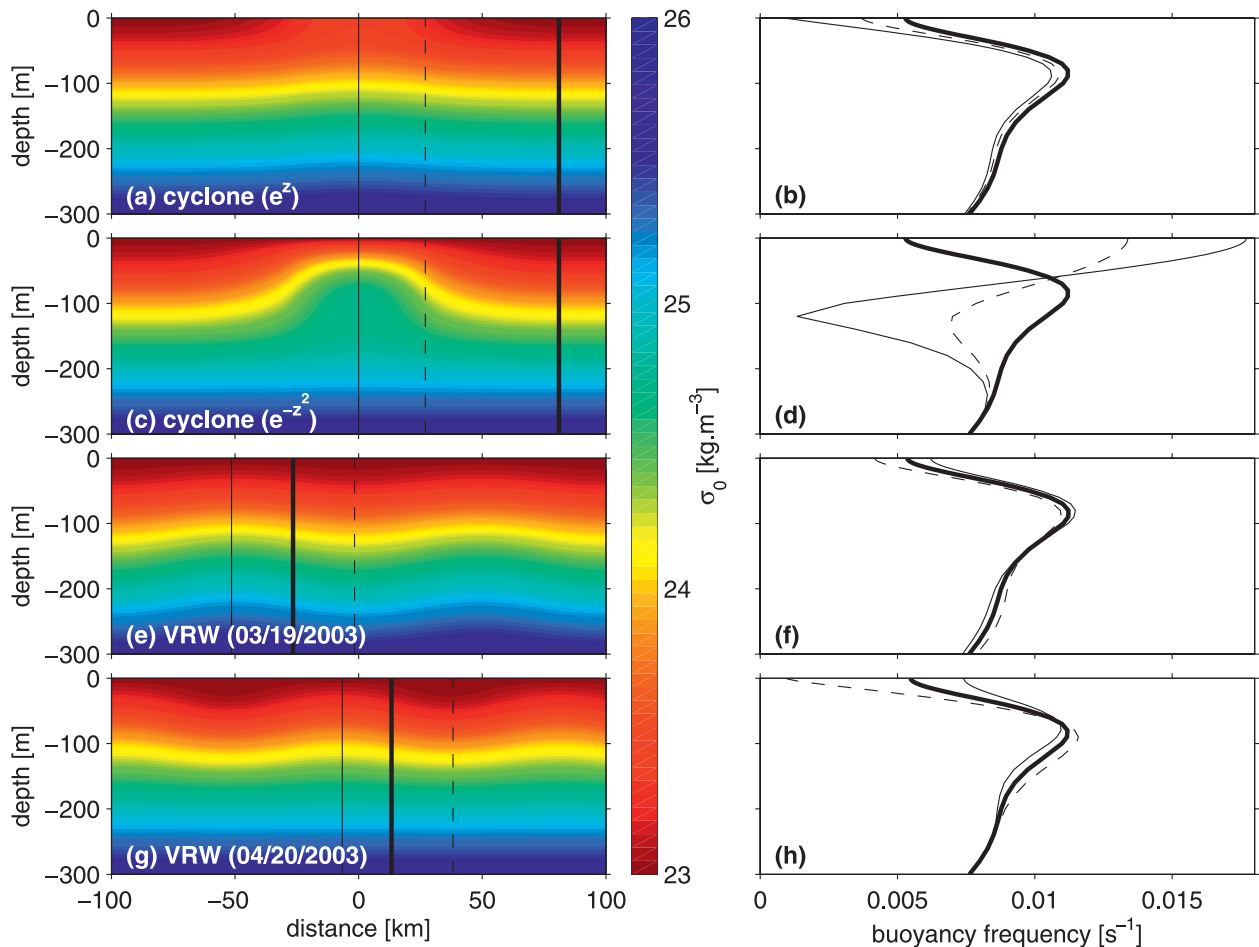
FIG. 7. (left) Vertical sections of potential density $\sigma_0$ and (right) buoyancy frequency profiles at different positions along the sections for the cyclone with (a),(b) exponential and (c),(d) Gaussian vertical structure and for the vorticity waves on (e),(f) 19 Mar and (g),(h) 20 Apr 2003. The positions of the buoyancy frequency profiles shown in (right) are indicated by the corresponding vertical lines in (left). The thick solid lines show the reference buoyancy frequency profile obtained from a 10-yr average of climatological observations.

Buoyancy frequency is reduced (enhanced) near the surface when the currents are switching direction from northwestward to southeastward (from southeastward to northwestward), when moving in the direction of propagation of the wave.

The parameters for the horizontal and vertical structures of the vorticity waves were chosen to yield inertially stable jets (e.g., Holton 1992, p. 281),

$$R_i > \frac{f}{f + \zeta}. \tag{11}$$

The rhs of (11) equals 1 where the vorticity is zero.

## 3. Propagation of internal tides through mesoscale currents

Potential generation locations of internal tidal rays were selected over Kaena Ridge and south of Oahu, where the topographic slopes were critical (equal to the $M_2$ internal characteristic slopes) and sloping upward toward the southwest side of the ridge. The initial directions of propagation were those maximizing the barotropically induced vertical currents, as predicted by a 3D primitive-equation numerical model of the tides, Primitive Equations Z-coordinate–Harmonic Analysis Tides (PEZHAT; Zaron et al. 2009). The initial wavelengths must also be specified. Nash et al. (2006) suggested that the internal tide's horizontal wavelength over Kaena Ridge may be set by the separation between generation regions on each side of the ridge, because the barotropic flow over the ridge simultaneously generates upward displacements of isopycnals on one side and downward displacements on the other side. The horizontal wavelength is therefore twice the ridge width, or ~50 km, corresponding to a vertical wavelength of 850 m, similar to that inferred from their observations. Because the ridge geometry varies in the Kauai Channel, the initial
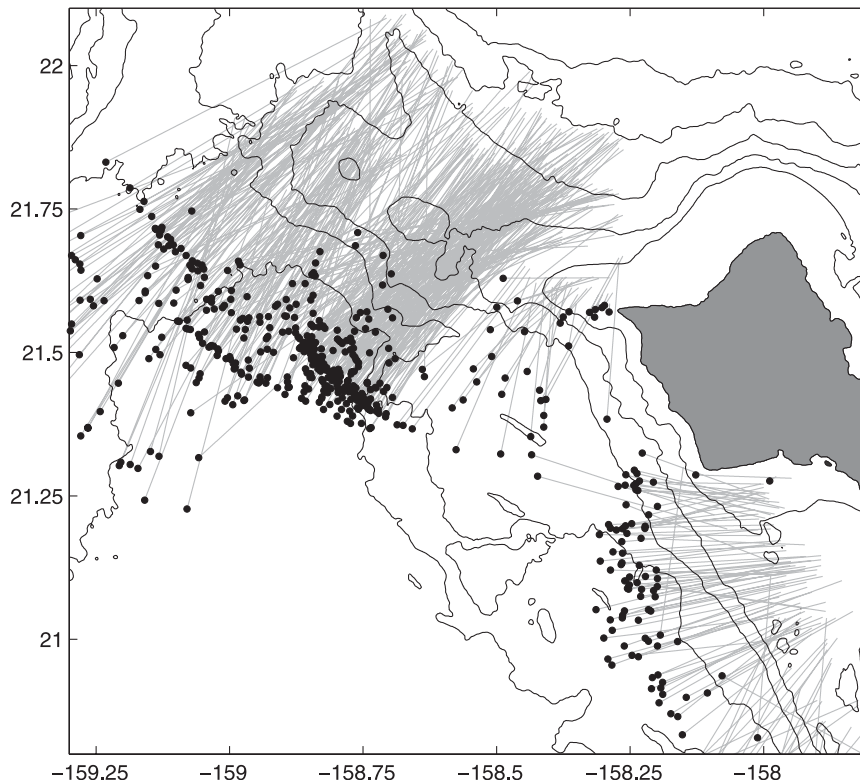
FIG. 8. Ray trajectories in a quiescent ocean. The rays originate at possible generation locations at critical topographic slopes over Kaena Ridge and south of Oahu. The black dots indicate where the rays reach the sea surface.

wavelengths should vary along the ridge; however, for simplicity, we set them to a constant value of 50 km here.

In the following subsections, we compare observations of surface semidiurnal currents with results from ray tracing. Phase-locked tidal currents were extracted from the high-pass-filtered currents (i.e., ''raw'' currents minus subinertial currents) by least squares fits over two 59-day periods, one in fall 2002 and one in spring 2003. Part I investigated the temporal variability of the semidiurnal tides by complex demodulating both the phase-locked tidal currents and the high-pass-filtered currents at semidiurnal frequencies (see Figs. 13 and 14 and section 5 of Part I for details) to separate the effects of interferences between semidiurnal tidal constituents (e.g., spring–neap cycle) from the effects of mesoscale currents on internal tide propagation.

We do not attempt here to infer the kinetic energy values at the surface from ray tracing because we do not know the initial energy level of the rays at their generation locations, nor do we consider all the possible generation locations and directions of propagation that contribute to the kinetic energy at a particular surface location. Instead, we focus on the ratio of the energy of rays propagating through background currents to the energy of rays

propagating in a quiescent ocean. We can then compare these ratios with the ratio of complex-demodulated semidiurnal kinetic energy of high-pass-filtered currents to the kinetic energy of phase-locked semidiurnal currents. Although the observed phase-locked semidiurnal currents differ from those numerically predicted in an ocean at rest (Part I), they are not likely to be affected by individual mesoscale features such as the cyclone on 29 September 2002, whose effects are filtered out by the least squares fit over the 59-day time series. In contrast, the high-pass-filtered currents contain the effects of each individual mesoscale feature.

Ray tracing is carried out (see the appendix for details on the equations and numerical schemes) until each ray reaches the sea surface or a critical layer (where the intrinsic frequency $\omega_0 = f$). Reflection effects cannot be addressed by ray tracing; however, if they merely consist of a superposition of oppositely traveling (in the vertical direction) waves, the energy ratio between rays propagating in the presence and absence of mesoscale currents should not be affected. The horizontal trajectories of rays propagating in a quiescent ocean are shown in Fig. 8. For the rays coming from Kaena Ridge, most of the surfacing locations occur between 30 and 45 km from the ridge

axis, consistent with the locations of enhanced surface kinetic energy in regional numerical models of the tides (Part I).

### a. Cyclone

The complex-demodulated semidiurnal kinetic energy on 29 September 2002 is shown in Fig. 9a for the high-pass-filtered currents and in Fig. 9b for the phase-locked currents. Their ratio is shown in Fig. 9c. The most striking feature is the much stronger kinetic energy near the cyclone core in the high-pass-filtered currents than in the phase-locked currents, observed at C1 by the moored ADCP and over the surrounding area by the HFRs. The maximum observed energy ratio is 15.5, and the energy ratio at C1 is 4.4 from the ADCP (12-m depth bin) compared with 2.6 from the HFR's closest grid cell (5 km away from C1).

The ratio of surface kinetic energy of rays propagating through the cyclone with a Gaussian vertical structure (Gaussian cyclone) to energy of rays propagating in a quiescent ocean is shown in Fig. 9d. Kinetic energy is increased at the surface near the vortex core, consistent with the observations. The maximum energy ratio obtained is 11.2, near the vortex center, and the energy ratio near C1 is 3.0, similar to the observed values. In contrast, for the cyclone with an exponential vertical structure (exponential cyclone), kinetic energy is reduced at the surface in the vortex core (Fig. 9e), contrary to observations. This highlights the extreme sensitivity of ray tracing to the vertical structure of the background currents. To investigate the sensitivity of the results to the choice of initial wavelength, we also used an initial horizontal wavelength of 25 km for ray tracing through the Gaussian cyclone (Fig. 9f). Some ray trajectories are farther diverted than for initial wavelengths of 50 km, but the pattern of increased energy within the cyclone core remains the same, although energy ratios reach much stronger values (viz., 43.6) near the vortex center.

To further illustrate the effects of mesoscale currents on internal tide propagation, some wave properties, along the ray with strongest negative Doppler shift in the presence of the Gaussian cyclone, are shown in Fig. 10. The ray surfaces on the edge of the cyclone core 15 km farther away from the ridge in the presence of the cyclone than in a quiescent ocean (Fig. 10a) because of advection and refraction by the background currents. The intrinsic frequency (the frequency in a frame of reference moving with the background currents) is reduced by a factor of 0.6 near the surface (Fig. 10c) but remains above $f$, so no critical layer is encountered for any of the rays considered. Because the intrinsic frequency decreases as the wave approaches the surface, the vertical group velocity is reduced [Eq. (A10)]. As a result, surfacing is

delayed by 5 h (Fig. 10b), corresponding to a 150° phase lag for $M_2$.

To understand what processes cause the energy to increase near the surface in the core of the cyclone, we compute the different terms of the energy balance equation (see the appendix for details),

$$\frac{dE}{dt} = -E\nabla \cdot \mathbf{C}_g + \frac{E}{\omega_0}\frac{d\omega_0}{dt}, \qquad (12)$$

where $E$ is the total energy (kinetic plus potential), $d/dt = \partial/\partial t + \mathbf{C}_g \cdot \nabla$ is the material derivative following the ray propagating at the group velocity $\mathbf{C}_g$, and $\omega_0$ is the intrinsic frequency. The first term on the rhs of (12) is the ray divergence contribution: when rays diverge ($\nabla \cdot \mathbf{C}_g > 0$), the energy decreases, whereas it increases when rays converge ($\nabla \cdot \mathbf{C}_g < 0$). The second term on the rhs of (12) is the energy exchanged with the background flow.

The evolution with depth of the terms in (12) is shown in Fig. 10d. In the absence of background currents, the intrinsic frequency is not Doppler-shifted, and the second term on the rhs of (12) is zero (thin dashed–dotted line). The energy variations (thin solid line) are therefore entirely caused by vertical divergence or convergence of rays (thin dashed line, indistinguishable from the thin solid line) because of the vertical gradients of buoyancy frequency. As a result, the energy evolution with depth follows the buoyancy frequency profile $N(z)$ [thin dotted line, indistinguishable from the thin solid line; see Eq. (A20) and Leaman and Sanford (1975)]. In contrast, in the presence of the cyclone, the energy evolution resulting from divergence or convergence of rays (thick dashed line) departs significantly from the buoyancy frequency profile (thick dotted line) because of the additional effect of horizontal refraction. Energy transfer with the background currents (thick dashed–dotted line) is negative, because the ray propagates in the direction of the current shear near the surface, causing its Doppler-shifted intrinsic frequency to decrease [Eq. (A7)]. Therefore, energy is transferred by the wave to the cyclone along this ray. However, note that for rays propagating from the ridge on the other side of the cyclone, where the vertical shear in the direction of propagation is reversed, energy is gained by the wave from the cyclone. Therefore, the net energy transfer between the internal tide and the cyclone depends on the position of the cyclone relative to the spatial variations of the internal wave energy. The amount of energy transferred to the cyclone along the ray shown in Fig. 10 is smaller than the amount of energy gained from ray convergence. As a result, the energy of the ray near the surface is stronger in the presence of the cyclone than in a quiescent ocean (cf. the thick and thin solid lines near the surface).
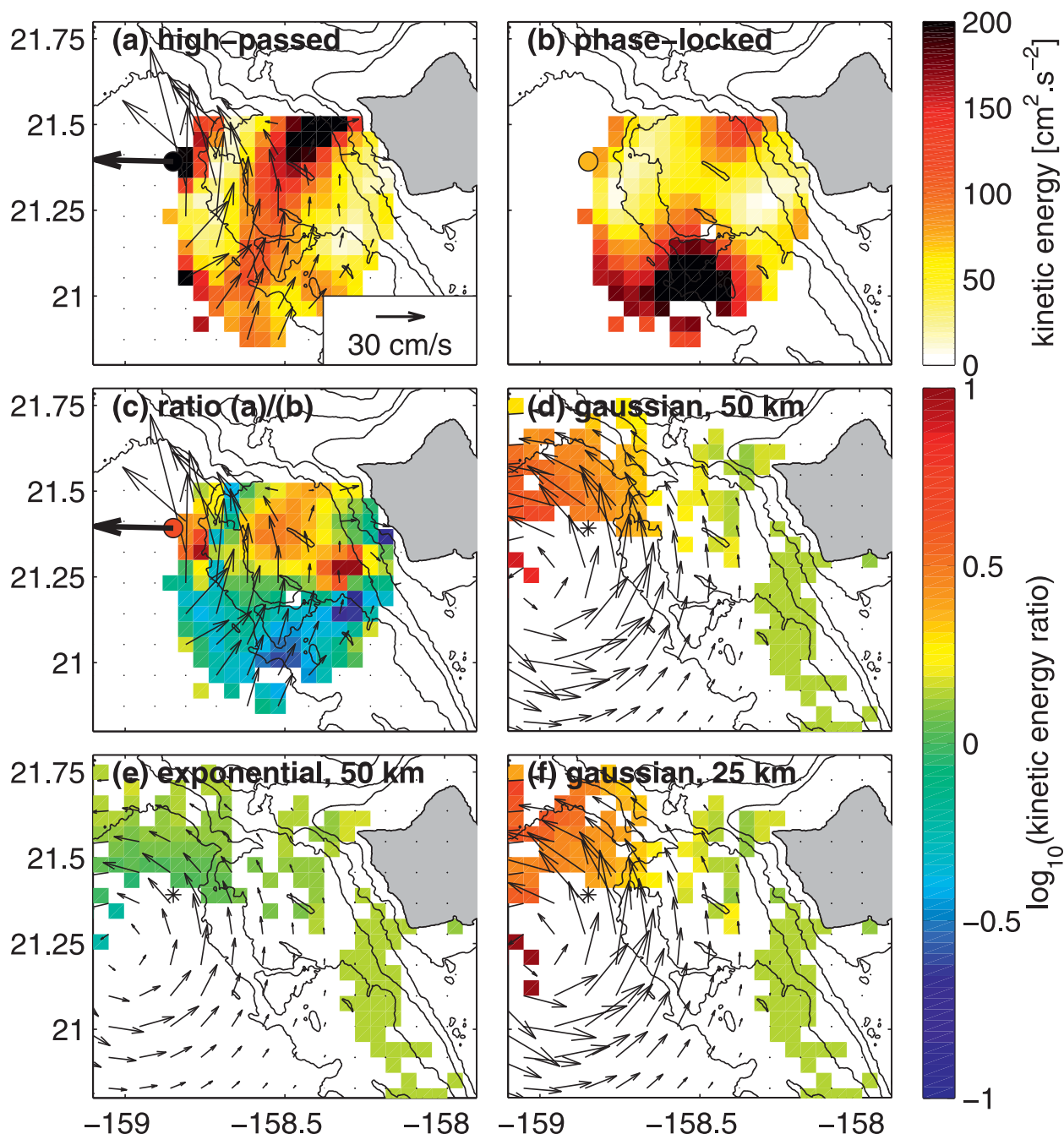
FIG. 9. Complex-demodulated semidiurnal surface kinetic energy on 29 Sep 2002, for (a) high-pass-filtered and (b) phase-locked currents. (c) The logarithm of the ratio of high-pass-filtered to phase-locked energy is shown. The logarithm of the ratio of surface energy of rays propagating through background currents to surface energy of rays propagating in a quiescent ocean are shown for the cyclone with (d) a Gaussian and (e) an exponential vertical structure. The initial horizontal wavelengths were set to 50 km. (f) For the cyclone with a Gaussian vertical structure, results are also shown for initial horizontal wavelengths set to 25 km. Energy ratios from ray tracing were binned onto the geographic grid of the idealized currents by taking the median value over all rays surfacing within each grid cell. Observations at mooring C1 (12-m depth bin) are shown by a colored circle and its location is indicated by a star in (d)–(f). Corresponding background surface currents are superimposed [except in (b)].
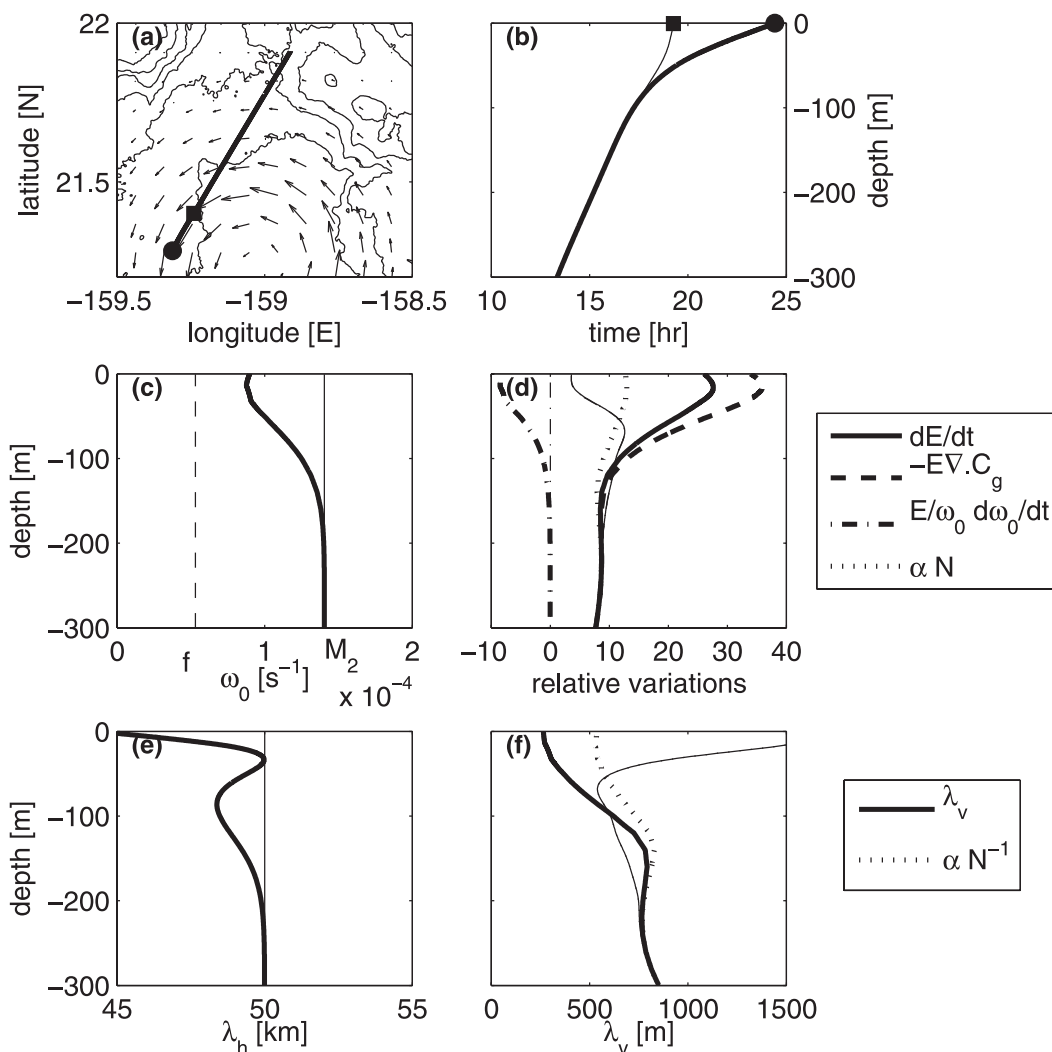
FIG. 10. Wave properties along the ray with strongest negative Doppler shift in the presence of the cyclone with a Gaussian vertical structure (thick lines), compared with the properties for the same ray propagating in a quiescent ocean (thin lines). (a) Horizontal trajectories until the rays reach the sea surface (indicated by a square for a quiescent ocean and a circle in the presence of the cyclone). Background surface currents are overlain. (b) Vertical trajectories as a function of time. (c) Intrinsic frequency vs depth (the thin dashed line indicates the inertial frequency). (d) Normalized relative evolution {e.g., $[dE/dt(z) - dE/dt(z_0)]/dE/dt(z_0)$, where $z_0$ is the depth at which the ray originates} of the terms in the energy balance Eq. (12): total energy variations (solid lines), ray divergence contribution (dashed lines), and energy transfer with mesoscale currents (dashed–dotted lines). The normalized relative buoyancy frequency profiles are shown by dotted lines. (e) Horizontal wavelength vs depth. (f) Vertical wavelength vs depth. The initial wavelength times $N(z_0)/N(z)$ are shown by dotted lines.

The evolution of the horizontal wavelength is shown in Fig. 10e. In the absence of background currents, the horizontal wavelength does not change (thin line), because the background state is horizontally homogeneous [see Eqs. (A11) and (A12)] and changes by less than 10% in the presence of the cyclone (thick line). In contrast, the vertical wavelength (Fig. 10f) changes significantly both in the absence and presence of background currents because of the vertical gradients of buoyancy frequency and refraction by the vertical shear. In

a quiescent ocean, the vertical wavelength reaches a minimum value of 540 m at 70-m depth and increases to 1600 m toward the surface (thin solid line), following the inverse of the buoyancy frequency profile $N(z)^{-1}$ [thin dotted line, indistinguishable from the thin solid line; see Eq. (A19)]. In the presence of the cyclone, the vertical wavelength reaches a minimum value of 265 m at the surface (thick solid line), 6 times smaller than in a quiescent ocean. Its evolution with depth departs from the inverse of the buoyancy frequency profile (thick dotted line).
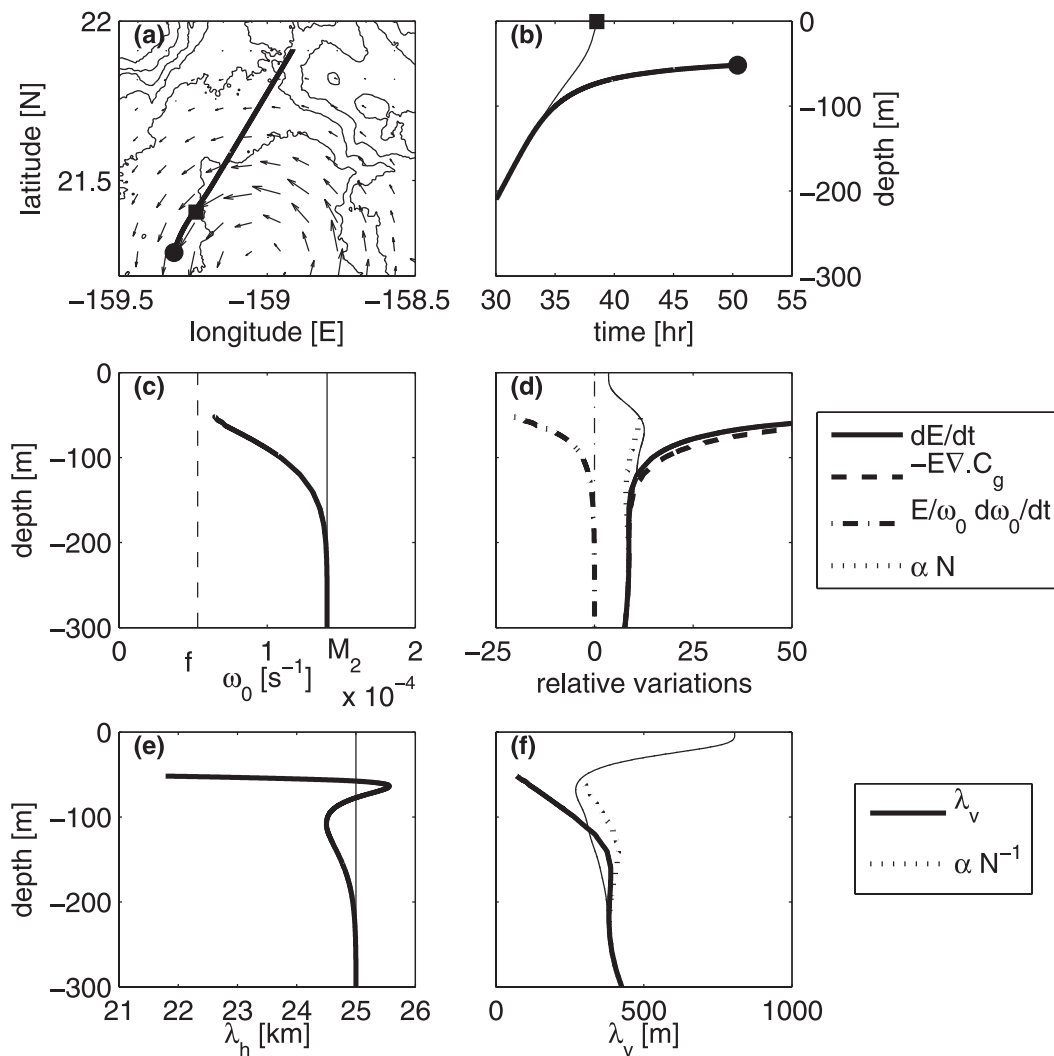
FIG. 11. As in Fig. 10, but for initial wavelengths set to 25 km instead of 50 km.

Although the surface energy pattern was not very sensitive to the choice of initial wavelengths (Fig. 9), the evolution of the ray shown in Fig. 10 is drastically modified when the initial horizontal wavelength is set to 25 km instead of 50 km (Fig. 11). Because of the increase in the horizontal wavenumber, the Doppler shift by the background currents is stronger and the intrinsic frequency approaches the inertial frequency limit $f$ (Fig. 11c). The vertical group velocity tends to zero [Eq. (A10)], and the ray is trapped below a critical level at ∼50-m depth (Fig. 11b; the integration of the ray equations was stopped after 50 h). As rays converge toward the critical depth, energy (Fig. 11d) tends to infinity (in the inviscid linear approximation), a fraction of which is transferred to the cyclone, and the vertical wavelength tends to zero (Fig. 11f). In reality, the internal wave may break before reaching the critical level while being partly reflected (see

the reviews by Staquet and Sommeria 2002; Edwards and Staquet 2005).

### b. Vorticity waves

The observations and results of ray tracing on 19 March 2003 are shown in Fig. 12. The complex-demodulated semidiurnal kinetic energy for the high-pass-filtered currents is weaker near the ridge and up to ∼40 km offshore but stronger farther offshore than for the phase-locked currents. This pattern is qualitatively reproduced by the ray-tracing model, except over the ridge near the island, where energy is slightly increased in the presence of the background currents, contrary to the observations. The observed increase of energy in the northwestern part of the HFR domain and at the moorings is not reproduced, but the observed currents differ strongly from the idealized currents there. The minimum observed energy
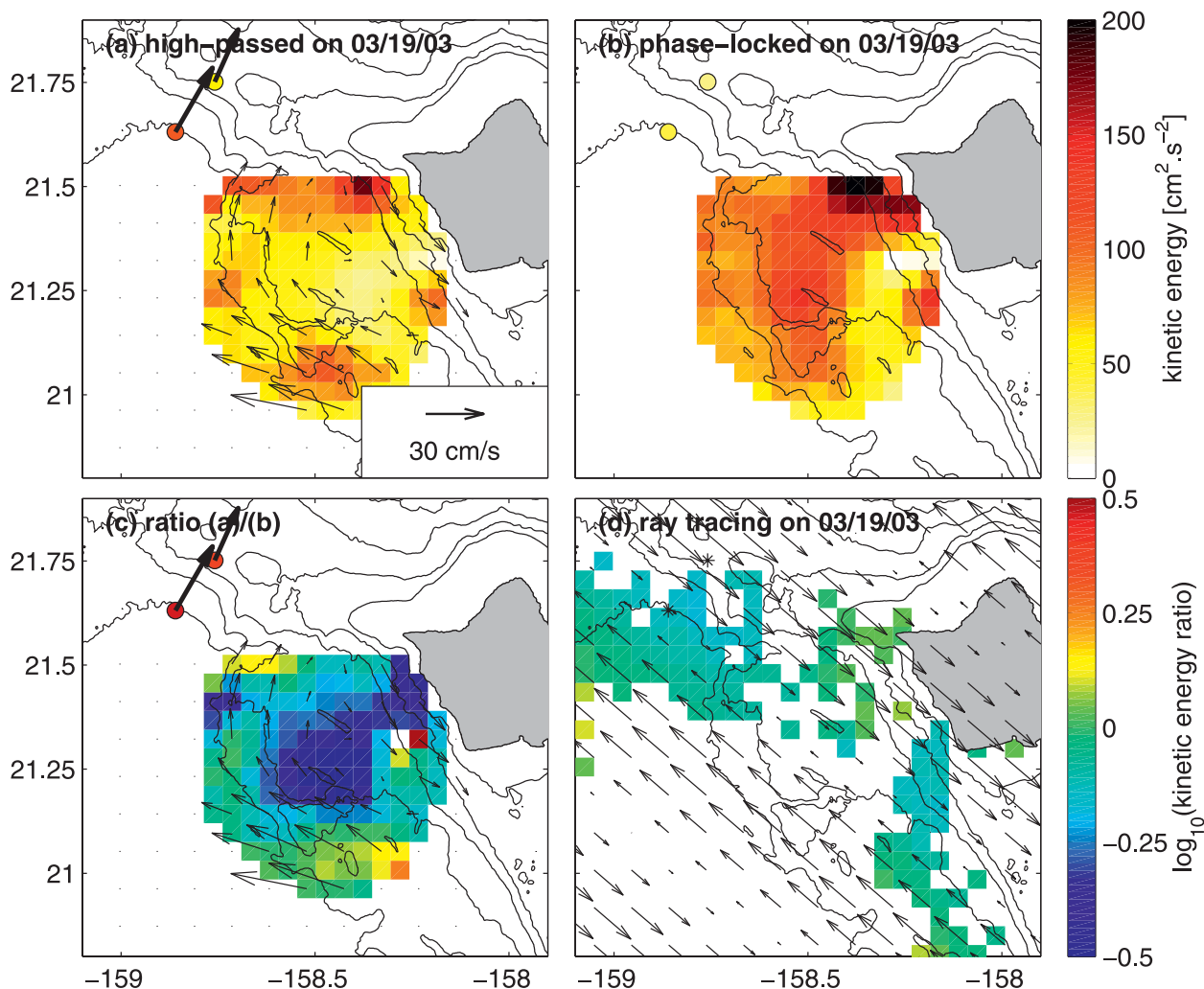
FIG. 12. Complex-demodulated semidiurnal surface kinetic energy on 19 Mar 2003 for (a) high-pass-filtered and (b) phase-locked currents. Logarithm of the ratio of (c) high-pass-filtered to phase-locked energy and (d) surface energy of rays propagating through background currents to surface energy of rays propagating in a quiescent ocean. Observations at mooring C2 and A2 (12-m depth bin) are shown by a colored circle and their locations are indicated by stars in (d). Corresponding background surface currents are superimposed [except in (b)].

ratio is 0.2, while the minimum energy ratio from ray tracing is only 0.65. As for the cyclone, the energy evolution in the vertical (not shown) is mainly caused by divergence or convergence of rays.

The opposite pattern occurs on 20 April (Fig. 13), when the vorticity wave is almost 180° out of phase with that on 19 March (Fig. 3). The observed pattern is qualitatively reproduced by the ray-tracing model, except again over the ridge near the island, where energy is reduced in the presence of the background currents, contrary to the observations. The maximum observed energy ratio is 3.1, while the maximum energy ratio from ray tracing is only 1.6. Therefore, the vorticity waves modulate the internal tide energy near the surface, through periodic

modifications of the background stratification, and may partly account for the incoherent variability of semidiurnal energy observed during spring 2003 in Part I.

## 4. Conclusions and broader implications

The effects of horizontally and vertically sheared mesoscale currents on internal tide propagation in the Kauai Channel were investigated using 3D ray tracing. The results are qualitatively consistent with observations of semidiurnal surface currents by high-frequency radars and moored ADCPs: a mesoscale cyclone causes the energy of internal tide rays propagating through its core to increase near the surface, and vorticity waves enhance
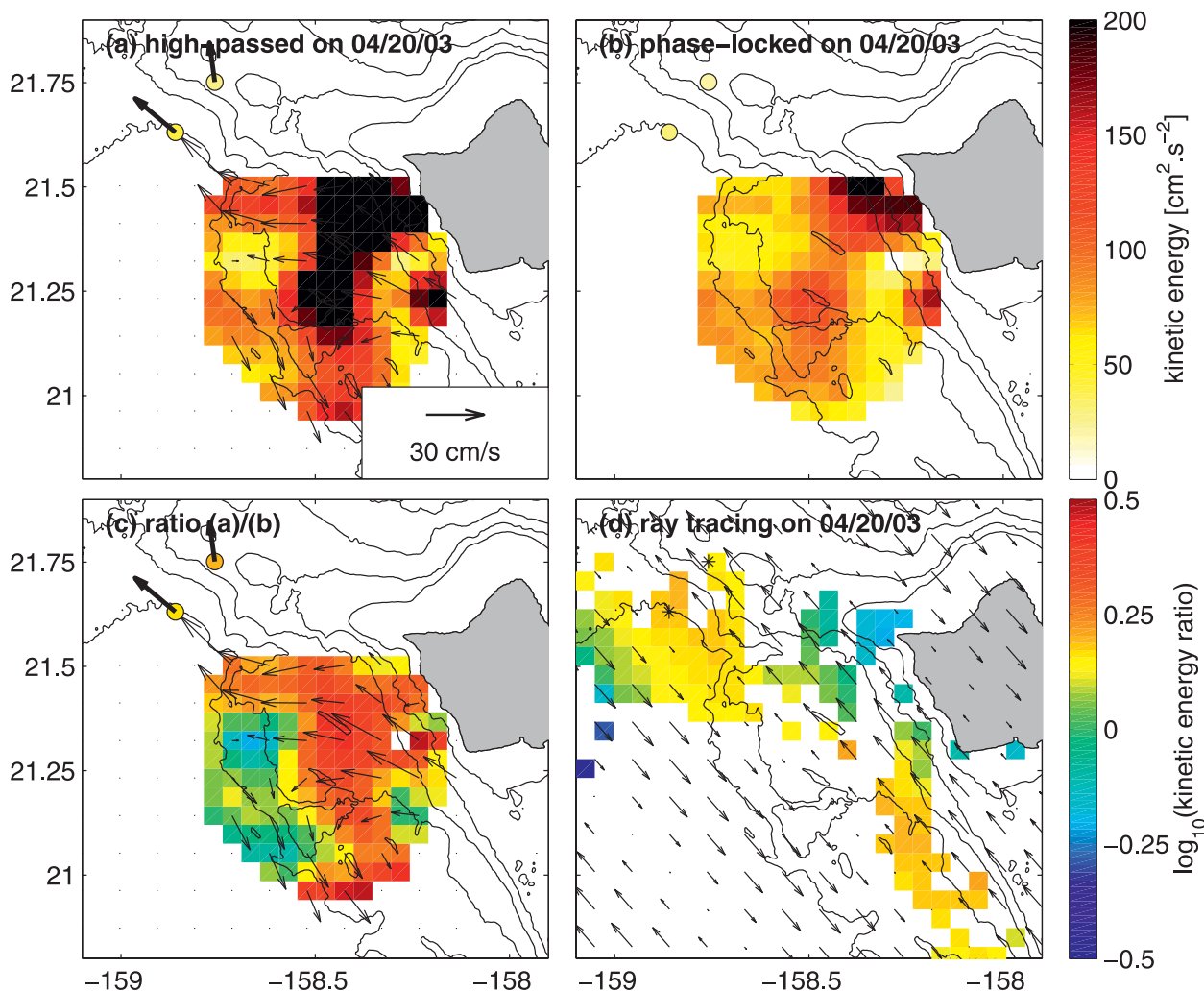
FIG. 13. As in Fig. 12, but for 20 Apr 2003.

or reduce the energy near the surface, depending on their phase. These examples illustrate the fact that, even close to their generation location, semidiurnal internal tides can become incoherent with astronomical forcing because of the presence of mesoscale variability. The kinetic energy is modulated principally by vertical and horizontal refraction caused by stratification variations associated with the mesoscale thermal or gradient winds and secondarily by energy transfers between the internal tides and background currents, due to Doppler shifting. In the case of the idealized mesoscale cyclone with a Gaussian vertical structure, energy can be amplified near the surface by a factor of 15 and the vertical wavelength can be reduced by a factor of 6, enhancing the vertical shear within the internal tide rays, which could trigger instabilities, wave breaking, and turbulent mixing.

Despite the obvious limitations of ray tracing when background current scales are similar to or even smaller than the wave scales (which is especially the case in the vertical direction) and the extreme sensitivity of ray tracing to the vertical structure of the background currents, the qualitative agreement between observations of semidiurnal surface currents in the Kauai Channel and ray-tracing predictions suggests that ray tracing may have captured the main effects that mesoscale currents have on internal tide propagation. Bender and Orszag (1999, chapter 10) already noted the good agreement between WKB approximations and exact solutions of some ordinary differential equations, even when the "small" parameter used in the approximation was $O(1)$. Nevertheless, our results should be considered with caution, until the effects on internal tide propagation of mesoscale currents such as those observed in the Kauai Channel
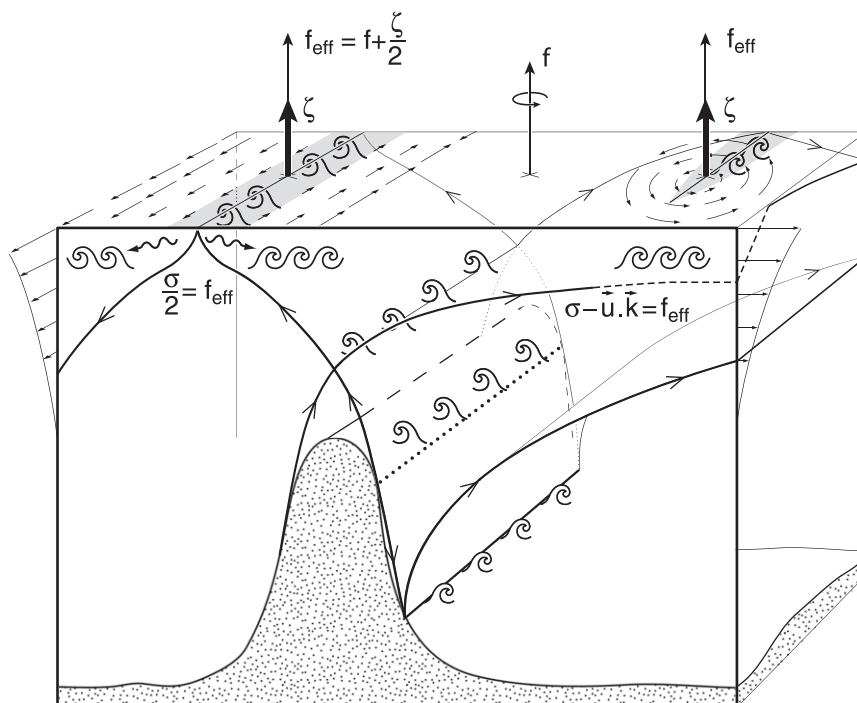
FIG. 14. Schematic representation of possible mixing locations (indicated by breaking waves) for internal tide sheets generated on the flanks of an ocean ridge in the presence of horizontally and vertically sheared mesoscale currents. Mixing can be triggered where energy is locally enhanced: at the generation locations over the ridge flanks, at the surface and bottom reflections, where rays propagating in different directions cross each other, and where ray tubes converge because of refraction by the inhomogeneous buoyancy frequency field. Mixing can also be triggered where the interactions of the internal waves with the background currents reduce the intrinsic frequency toward the (effective) inertial frequency limit (critical levels). Internal waves generated by parametric subharmonic instability of the internal tides (with half the frequency) are shown by wiggly vectors.

are investigated with primitive equation models. Dunphy (2009) investigated the effect of mesoscale eddies on internal tides in idealized simulations using the Massachusetts Institute of Technology general circulation model (MITgcm). He showed that eddies were generating interference patterns in their wakes as the internal tides propagated through them, but he did not investigate the effects on the internal tides within the eddies. Some studies have incorporated background baroclinic currents into regional numerical models of the tides (e.g., Pereira et al. 2002, 2007; Padman et al. 2009), and Arbic et al. (2010) recently implemented the first global model that simultaneously resolves the eddying general circulation and the barotropic and baroclinic tides.

If the ray-tracing method used here is proved to be qualitatively correct even when the scale separation requirement is not fulfilled, it could provide a computationally cheaper alternative to primitive equation models for studying the effects of mesoscale currents

on internal tide propagation. For example, the method could be used to revisit the observations of Chiswell (2002) and help to quantify how much of the semidiurnal amplitude and phase variability at Station ALOHA is due to refraction and Doppler shifting by the mesoscale currents, as opposed to changes in generation efficiency, with implications on estimations of the baroclinic tidal energy flux radiating from the Hawaiian Islands.

We have not taken into account the effects of modifications of the effective Coriolis and buoyancy frequencies by the background shears (Mooers 1975b; Kunze 1985), which were not necessary to interpret our observations. However, these additional effects could have a significant impact on semidiurnal internal tide propagation in regions of strongly sheared flows, such as western boundary currents, or at higher latitudes, where semidiurnal frequencies are closer to the inertial frequency. Pereira et al. (2007) showed that internal tides were trapped on the negative vorticity side of the Brazil Current and reflected on its positive vorticity side, with implications

on tidally induced mixing, in a primitive equation model of the South Brazil Bight. Hosegood and van Haren (2006) observed that intermittency of semidiurnal internal tides in the Faeroe–Shetland Channel appeared to be related to variability in the background stratification and the low-frequency vorticity, which had a magnitude sufficient to increase the effective Coriolis frequency above $M_2$. The modification of the effective Coriolis and buoyancy frequencies by the background shears could be easily implemented in the ray-tracing method.

We speculate that the effects of mesoscale currents on internal tide propagation could smear out the critical latitudes of 28.9° for $M_2/2$ internal waves generated by parametric subharmonic instability of the $M_2$ internal tides (MacKinnon and Winters 2005) and of 74.5° for the latter into broad latitudinal bands, with implications on our understanding of where internal wave-induced mixing should take place in the ocean. Some of the relevant processes are sketched in Fig. 14.

## APPENDIX

### 3D Ray Tracing through Mesoscale Currents

#### a. Dispersion relation

Suppose internal waves are governed by the inviscid, adiabatic, hydrostatic, Boussinesq equations linearized around a background state:

$$\frac{Du}{Dt} + u\frac{\partial U}{\partial x} + v\frac{\partial U}{\partial y} + w\frac{\partial U}{\partial z} - fv = -\frac{1}{\rho_0}\frac{\partial p}{\partial x}, \quad (A1)$$

$$\frac{Dv}{Dt} + u\frac{\partial V}{\partial x} + v\frac{\partial V}{\partial y} + w\frac{\partial V}{\partial z} + fu = -\frac{1}{\rho_0}\frac{\partial p}{\partial y}, \quad (A2)$$

$$0 = -\frac{1}{\rho_0}\frac{\partial p}{\partial z} - b, \quad (A3)$$

$$\frac{\partial u}{\partial x} + \frac{\partial v}{\partial y} + \frac{\partial w}{\partial z} = 0, \quad \text{and} \quad (A4)$$

$$\frac{Db}{Dt} + u\frac{\partial B}{\partial x} + v\frac{\partial B}{\partial y} - N^2 w = 0, \quad (A5)$$

where $u$, $v$, $w$, $p$, and $b$ are the zonal, meridional, and vertical components of velocity and the pressure and buoyancy fields describing the internal waves; $U$, $V$, $W$, and $B$ are the corresponding fields describing the background state; $f$ is the Coriolis parameter; $\rho_0$ is a reference density; $N^2 = N_0^2 - \partial B/\partial z$ is the buoyancy frequency squared of the background state, where $N_0$ is the buoyancy frequency of the ocean at rest; and $D/Dt = \partial/\partial t + \mathbf{U} \cdot \mathbf{V}$ is the material derivative.

This is a closed system of five equations for five unknowns, with nonhomogeneous coefficients. Following Olbers (1981b), we neglect the gradients of the background state (except for the contribution of the vertical gradient of buoyancy to the background buoyancy frequency) and solve for local plane waves solutions,

$$(u, v, w, p, b) = \text{Re}[(u_0, v_0, w_0, p_0, b_0)e^{i(\mathbf{k}\cdot\mathbf{x}-\omega t)}], \quad (A6)$$

where $\mathbf{k} = (k, l, m)$ is the local wavenumber vector and $\omega$ is the local frequency.

We obtain the local dispersion relation,

$$\omega = \Omega(\mathbf{k}, \mathbf{x}, t) = \omega_0 + \mathbf{k} \cdot \mathbf{U}, \quad (A7)$$

where the intrinsic frequency $\omega_0 = \Omega_0(\mathbf{k}, \mathbf{x}, t)$ satisfies the classic dispersion relation for hydrostatic internal waves,

$$\omega_0^2 = f^2 + N^2 \frac{k^2 + l^2}{m^2}. \quad (A8)$$

Locally, the only effect of the background state is to modify the buoyancy frequency and to Doppler shift the intrinsic frequency of the wave.

#### b. Propagation and refraction

As the wave propagates through the varying background state, its wavenumber and frequency adjust to satisfy the dispersion relation and the wave gets refracted. Its trajectory is governed by the propagation equation,

$$\frac{d\mathbf{x}}{dt} = \mathbf{C}_g = \frac{\partial \Omega}{\partial \mathbf{k}} = \mathbf{C}_{g0} + \mathbf{U}, \qquad (A9)$$

where $\mathbf{C}_g$ is the group velocity and $d/dt = \partial/\partial t + \mathbf{C}_g \cdot \nabla$. The intrinsic group velocity is

$$\mathbf{C}_{g0} = \frac{\partial \Omega_0}{\partial \mathbf{k}} = \left( \frac{N^2 k}{\omega_0 m^2}, \frac{N^2 l}{\omega_0 m^2}, -\frac{\omega_0^2 - f^2}{\omega_0 m} \right). \qquad (A10)$$

Its wavenumber evolution is governed by the refraction equation,

$$\frac{d\mathbf{k}}{dt} = \mathbf{r} = -\frac{\partial \Omega}{\partial \mathbf{x}} = \mathbf{r}_0 - k \frac{\partial U}{\partial \mathbf{x}} - l \frac{\partial V}{\partial \mathbf{x}} - m \frac{\partial W}{\partial \mathbf{x}}, \qquad (A11)$$

where $\mathbf{r}$ is the rate of refraction, and the intrinsic rate of refraction is

$$\mathbf{r}_0 = -\frac{\partial \Omega_0}{\partial \mathbf{x}} = -\frac{\omega_0^2 - f^2}{\omega_0 N} \frac{\partial N}{\partial \mathbf{x}}. \qquad (A12)$$

Finally, the evolution of frequency is governed by

$$\frac{d\omega}{dt} = \frac{\partial \Omega}{\partial t}, \qquad (A13)$$

and is negligible when the background flow varies on time scales much longer than the time it takes the waves to propagate through it ("frozen" background state). In this case, $\omega$ can be considered constant when following the wave packet.

*c. Energy evolution*

In the hydrostatic approximation ($f^2, \omega_0^2 \ll N^2$), the kinetic energy is well approximated by the horizontal kinetic energy,

$$\mathrm{KE} \approx \mathrm{HKE} = \frac{1}{2} \rho_0 \overline{|u|^2 + |v|^2}, \qquad (A14)$$

where the overbar denotes time averaging and $|\ |$ denotes the absolute value. The potential energy is given by

$$\mathrm{PE} = \frac{1}{2} \rho_0 \frac{\overline{|b|^2}}{N^2}. \qquad (A15)$$

The ratio of kinetic energy over total energy $E = \mathrm{KE} + \mathrm{PE}$ is

$$\frac{\mathrm{KE}}{E} = \frac{1}{2} \frac{\omega_0^2 + f^2}{\omega_0^2}. \qquad (A16)$$

The evolution of total energy is governed by the conservation of wave action, $A = E/\omega_0$ (Bretherton and Garrett 1968),

$$\frac{\partial A}{\partial t} + \nabla \cdot (\mathbf{C}_g A) = 0, \qquad (A17)$$

which means that the action enclosed in a small volume moving along a ray with the group velocity is conserved. Equation (A17) can be rewritten as an energy balance equation,

$$\frac{dE}{dt} = -E \nabla \cdot \mathbf{C}_g + \frac{E}{\omega_0} \frac{d\omega_0}{dt}, \qquad (A18)$$

where the first term on the rhs is the ray divergence contribution: when rays diverge ($\nabla \cdot \mathbf{C}_g > 0$), the energy decreases, whereas it increases when rays converge ($\nabla \cdot \mathbf{C}_g < 0$). In the absence of background currents, the buoyancy frequency is horizontally homogeneous, and Eqs. (A11) and (A12) imply that $k$ and $l$ are constant. Furthermore, Eq. (A7) implies that $\omega_0$ is also constant. It follows from Eq. (A8) that

$$m = m(z) \propto N(z), \qquad (A19)$$

and from Eqs. (A17), (A10), and (A19) that

$$E = E(z) \propto \frac{1}{\mathbf{C}_{g0z}} \propto m \propto N(z). \qquad (A20)$$

In the presence of background currents, energy is also affected by horizontal variations of $N$ and $m$, as well as the 3D variations of $k$, $l$, and $\omega_0$. The energy evolution resulting from ray divergence can be obtained from Eq. (A17),

$$\nabla \cdot \mathbf{C}_g = -\frac{1}{A} \frac{dA}{dt}. \qquad (A21)$$

The second term on the rhs of Eq. (A18) is the energy exchanged with the background flow: when the waves propagate upward in the direction of the shear, the Doppler-shifted intrinsic frequency decreases [Eq. (A7)], so $E/\omega_0 \, d\omega_0/dt < 0$ and energy is transferred from the waves to the background flow. Conversely, when the waves propagate upward against the shear, the intrinsic frequency increases, so $E/\omega_0 \, d\omega_0/dt > 0$ and energy is transferred from the background flow to the waves. The opposite happens for a downward-propagating wave. This term is obtained from the evolution of intrinsic frequency along the ray, given by (A7). To interpret its physical meaning, we derive it explicitly by obtaining the energy equation from Eqs. (A1)–(A5), and comparing to Eq. (A18),

$$\frac{E}{\omega_0}\frac{d\omega_0}{dt} = \rho_0 \mathrm{Re}\left[\overline{u^*u_i}\frac{\partial U}{\partial x_i} + \overline{v^*u_i}\frac{\partial V}{\partial x_i} - \frac{|b|^2}{2N^4}\left(\frac{\partial U}{\partial z}\frac{\partial B}{\partial x} + \frac{\partial V}{\partial z}\frac{\partial B}{\partial y}\right) + \frac{\overline{u^*b}}{N^2}\frac{\partial B}{\partial x} + \frac{\overline{v^*b}}{N^2}\frac{\partial B}{\partial y}\right], \quad \text{(A22)}$$

where the asterisk denotes the complex conjugate and the repeated indices *i* are implicitly summed from 1 to 3. The first two terms on the rhs of Eq. (A22) are the rate of working of the radiation stress tensor of the waves against the rate of strain of the background flow (Garrett 1968). Additional terms appear as a result of the horizontal gradients of stratification.

### d. Numerical implementation

The evolution equations for position and wavenumber [Eqs. (A9)–(A12)] are integrated numerically using the fourth-order Runge–Kutta finite difference scheme, except for the vertical wavenumber, which is computed directly from Eq. (A8). This ensures that the dispersion relation is always exactly satisfied and reduces the errors introduced by the numerical integration.

Following Edwards and Staquet (2005), we compute the evolution of the action along a ray by computing the volume of a small tetrahedron moving along each ray. Therefore, for each generation location, we compute the paths of four rays forming the vertices of an initially regular tetrahedron with 10-m-long edges. The position and wavenumber of the ray are obtained by averaging over the four rays. The integration time steps are chosen such that the maximum horizontal displacements are equal to half the initial tetrahedron edge length (i.e., 5 m), yielding stable results for energy estimation. The energy thus estimated was compared with that obtained from Eq. (A20) in the case of a quiescent ocean, with discrepancies smaller than 6%.

## REFERENCES

Arbic, B. K., A. J. Wallcraft, and E. J. Metzger, 2010: Concurrent simulation of the eddying general circulation and tides in a global ocean model. *Ocean Modell., 32,* 175–187.

Bender, C. M., and S. A. Orszag, 1999: *Advanced Mathematical Methods for Scientists and Engineers.* Springer-Verlag, 593 pp.

Blumen, W., 1978: Uniform potential vorticity flow: Part I. Theory of wave interactions and two-dimensional turbulence. *J. Atmos. Sci., 35,* 774–783.

Bretherton, F. P., 1966: The propagation of groups of internal gravity waves in a shear flow. *Quart. J. Roy. Meteor. Soc., 92,* 466–480.

——, and C. J. Garrett, 1968: Wavetrains in inhomogeneous moving media. *Proc. Roy. Soc. London, 302,* 529–554.

Bühler, O., and M. E. McIntyre, 2005: Wave capture and wave-vortex duality. *J. Fluid Mech., 534,* 67–95.

Carter, G. S., and Coauthors, 2008: Energetics of $M_2$ barotropic-to-baroclinic tidal conversion at the Hawaiian Islands. *J. Phys. Oceanogr., 38,* 2205–2223.

Chavanne, C., 2007: Observations of the impact of mesoscale currents on internal tide propagation. Ph.D. thesis, University of Hawaii at Manoa, 198 pp.

——, P. Flament, G. Carter, M. Merrifield, D. Luther, E. Zaron, and K.-W. Gurgel, 2010: The surface expression of semidiurnal internal tides near a strong source at Hawaii. Part I: Observations and numerical predictions. *J. Phys. Oceanogr., 40,* 1155–1179.

Chiswell, S. M., 2002: Energy levels, phase, and amplitude modulation of the baroclinic tide off Hawaii. *J. Phys. Oceanogr., 32,* 2640–2651.

Dunphy, M., 2009: The influence of mesoscale eddies on the internal tide. M.S. thesis, Department of Applied Mathematics, University of Waterloo, 107 pp.

Eakins, B. W., J. E. Robinson, T. Kanamatsu, J. Naka, J. R. Smith, E. Takahashi, and D. A. Clague, 2003: Hawaii's volcanoes revealed. U. S. Geological Survey, Geological Investigations Series Map I-2809.

Edwards, N. R., and C. Staquet, 2005: Focusing of an inertia-gravity wave packet by a baroclinic shear flow. *Dyn. Atmos. Oceans, 40,* 91–113.

Garrett, C. J. R., 1968: On the interaction between internal gravity waves and a shear flow. *J. Fluid Mech., 34,* 711–720.

Griffiths, S. D., and R. H. J. Grimshaw, 2007: Internal tide generation at the continental shelf modeled using a modal decomposition: Two-dimensional results. *J. Phys. Oceanogr., 37,* 428–451.

Held, I. M., R. T. Pierrehumbert, S. T. Garner, and K. L. Swanson, 1995: Surface quasi-geostrophic dynamics. *J. Fluid Mech., 282,* 1–20.

Holton, J. R., 1992: *An Introduction to Dynamic Meteorology.* Academic Press, 511 pp.

Hosegood, P., and H. van Haren, 2006: Sub-inertial modulation of semi-diurnal currents over the continental slope in the Faeroe-Shetland Channel. *Deep-Sea Res., 53,* 627–655.

Jones, R. M., 2001: The dispersion relation for internal acoustic-gravity waves in a baroclinic fluid. *Phys. Fluids, 13,* 1274–1280.

——, 2005: A general dispersion relation for internal gravity waves in the atmosphere or ocean, including baroclinicity, vorticity, and the rate of strain. *J. Geophys. Res., 110,* D22106, doi:10.1029/2004JD005654.

Jones, W. L., 1969: Ray tracing for internal gravity waves. *J. Geophys. Res., 74,* 2028–2033.

Karl, D. M., and R. Lukas, 1996: The Hawaii Ocean Time-series (HOT) program: Background, rationale and field implementation. *Deep-Sea Res., 43,* 129–156.

Kunze, E., 1985: Near-inertial wave propagation in geostrophic shear. *J. Phys. Oceanogr., 15,* 544–565.

Lapeyre, G., and P. Klein, 2006: Dynamics of the upper oceanic layers in terms of surface quasigeostrophy theory. *J. Phys. Oceanogr., 36,* 165–176.

Leaman, K. D., and T. B. Sanford, 1975: Vertical energy propagation of inertial waves: A vector spectral analysis of velocity profiles. *J. Geophys. Res., 80,* 1975–1978.

MacKinnon, J. A., and K. B. Winters, 2005: Subtropical catastrophe: Significant loss of low-mode tidal energy at 28.9°. *Geophys. Res. Lett., 32,* L15605, doi:10.1029/2005GL023376.

Martin, J. P., D. L. Rudnick, and R. Pinkel, 2006: Spatially broad observations of internal waves in the upper ocean at the Hawaiian Ridge. *J. Phys. Oceanogr.,* **36,** 1085–1103.

Mooers, C. N. K., 1975a: Several effects of a baroclinic current on the cross-stream propagation of inertial-internal waves. *Geophys. Fluid Dyn.,* **6,** 242–275.

——, 1975b: Several effects of baroclinic currents on the three-dimensional propagation of inertial-internal waves. *Geophys. Fluid Dyn.,* **6,** 277–284.

Moulin, F. Y., and J.-B. Flór, 2006: Vortex-wave interaction in a rotating stratified fluid: WKB simulations. *J. Fluid Mech.,* **563,** 199–222.

Müller, P., 1976: On the diffusion of momentum and mass by internal gravity waves. *J. Fluid Mech.,* **77,** 789–823.

Nash, J. D., E. Kunze, C. M. Lee, and T. B. Sanford, 2006: Structure of the baroclinic tide generated at Kaena Ridge, Hawaii. *J. Phys. Oceanogr.,* **36,** 1123–1135.

Olbers, D. J., 1981a: A formal theory of internal wave scattering with applications to ocean fronts. *J. Phys. Oceanogr.,* **11,** 1078–1099.

——, 1981b: The propagation of internal waves in a geostrophic current. *J. Phys. Oceanogr.,* **11,** 1224–1233.

Padman, L., S. L. Howard, A. H. Orsi, and R. D. Muench, 2009: Tides of the northwestern Ross Sea and their impact on dense outflows of Antarctic Bottom Water. *Deep-Sea Res.,* **56,** 818–834.

Park, J.-H., and D. R. Watts, 2006: Internal tides in the southwestern Japan/East Sea. *J. Phys. Oceanogr.,* **36,** 22–34.

Pereira, A. F., A. Beckmann, and H. H. Hellmer, 2002: Tidal mixing in the southern Weddell Sea: Results from a three-dimensional model. *J. Phys. Oceanogr.,* **32,** 2151–2170.

——, B. M. Castro, L. Calado, and I. C. A. da Silveira, 2007: Numerical simulation of $M_2$ internal tides in the South Brazil Bight and their interaction with the Brazil Current. *J. Geophys. Res.,* **112,** C04009, doi:10.1029/2006JC003673.

Pinkel, R., and D. Rudnick, 2006: Editorial. *J. Phys. Oceanogr.,* **36,** 965–966.

Polzin, K. L., 2008: Mesoscale eddy–internal wave coupling. Part I: Symmetry, wave capture, and results from the Mid-Ocean Dynamics Experiment. *J. Phys. Oceanogr.,* **38,** 2556–2574.

Rainville, L., and R. Pinkel, 2006: Propagation of low-mode internal waves through the ocean. *J. Phys. Oceanogr.,* **36,** 1220–1236.

Rudnick, D. L., and Coauthors, 2003: From tides to mixing along the Hawaiian Ridge. *Science,* **301,** 355–357.

Staquet, C., and J. Sommeria, 2002: Internal gravity waves: From instabilities to turbulence. *Annu. Rev. Fluid Mech.,* **34,** 559–593.

Young, W. R., and M. Ben Jelloul, 1997: Propagation of near-inertial oscillations through a geostrophic flow. *J. Mar. Res.,* **55,** 735–766.

Zaron, E. D., C. Chavanne, G. D. Egbert, and P. Flament, 2009: Baroclinic tidal generation in the Kauai Channel inferred from high-frequency radio Doppler current meters. *Dyn. Atmos. Oceans,* **48,** 93–120.